PNAS INAUGURAL ARTICLE | ENGINEERING OPEN ACCESS

Integrating chemistry, fluid flow, and mechanics to drive spontaneous formation of three-dimensional (3D) patterns in anchored microstructures

Moslem Moradi[a], Oleg E. Shklyaev[a], and Anna C. Balazs[a,1]

This contribution is part of the special series of Inaugural Articles by members of the National Academy of Sciences elected in 2021.
Contributed by Anna C. Balazs; received November 10, 2023; accepted January 17, 2024; reviewed by Ryan C. Hayward and Meredith Silberstein

Enzymatic reactions in solution drive the convection of confined fluids throughout the enclosing chambers and thereby couple the processes of reaction and convection. In these systems, the energy released from the chemical reactions generates a force, which propels the fluids' spontaneous motion. Here, we use theoretical and computational modeling to determine how reaction-convection can be harnessed to tailor and control the dynamic behavior of soft matter immersed in solution. Our model system encompasses an array of surface-anchored, flexible posts in a millimeter-sized, fluid-filled chamber. Selected posts are coated with enzymes, which react with dissolved chemicals to produce buoyancy-driven fluid flows. We show that these chemically generated flows exert a force on both the coated (active) and passive posts and thus produce regular, self-organized patterns. Due to the specificity of enzymatic reactions, the posts display controllable kaleidoscopic behavior where one regular pattern is smoothly morphed into another with the addition of certain reactants. These spatiotemporal patterns also form "fingerprints" that distinctly characterize the system, reflecting the type of enzymes used, placement of the enzyme-coated posts, height of the chamber, and bending modulus of the elastic posts. The results reveal how reaction-convection provides concepts for designing soft matter that readily switches among multiple morphologies. This behavior enables microfluidic devices to be spontaneously reconfigured for specific applications without construction of new chambers and the fabrication of standalone sensors that operate without extraneous power sources.

reaction-convection | spatiotemporal pattern formation | chemically active posts

Enzymatic reactions in solution can produce density gradients that trigger the spontaneous flow of the surrounding fluid. If flexible materials are submerged in this solution, then the generated flow and corresponding forces could work as a "tool" to modify the material's shape and temporal behavior in controllable ways. Moreover, the energy realized from the reaction provides the fuel to run the entire process. To date, there have been few studies on using this chemically generated flow to actuate the motion and reconfiguration of soft deformable materials in solution (1–8). What is missing from generalizing and realizing this self-driven functioning is a set of design rules to interconnect the type of enzyme, the generated flow pattern, and the material's flexibility with the resultant morphology and dynamics of the fashioned material. As a step toward achieving this goal, we develop a computational model for the behavior of a square array of elastic micro-posts anchored to the bottom of a fluid-filled chamber and coated with different enzymes. The posts can bend but cannot alter their location in the chamber. With this reduced degree of freedom, the immobile posts constitute relatively simple starting materials for determining the necessary correlations within the system. Consequently, we use our model to investigate the ability of enzymatic reactions on the posts to generate fluid flows that control the dynamic structure and pattern formation within the array. For a system encompassing at least two different enzymatic coatings, we show that the array displays "kaleidoscopic" patterns and dynamics when the appropriate chemical reactants are added sequentially to the solution. For relatively large arrays, the type of enzymes, the number of decorated posts and their relative placement in the array provide innumerable choices (even assuming fixed values for the posts' flexibility and the chamber height). Once this choice is made, however, each system organizes into a singular, well-defined pattern, i.e., the array exhibits a characteristic "fingerprint" (which persists until the reactants are consumed but can be revived with fresh reagents). The distinctive fingerprint evolves from the dynamic interactions among the chemical constituents, the chemically generated fluid flow, the placement of the active posts, and the fluid-structure interactions between the flowing fluid and all the posts. A change in just one of the parameters leads to new dynamic behavior,

Significance

Through modeling, we show that enzymatic reactions on flexible microposts in solution inherently generate reaction-convection processes, which provide untapped approaches for regulating the spatiotemporal behavior of soft matter in fluids. Through self-generated fluid flows, the posts form distinct "fingerprints" that characterize the properties of that given system. Each variation in the system's features leads to the formation of a different fingerprint. Hence, the system constitutes a sensor, allowing specific chemicals to be identified through the formation of specific patterns. The posts also display kaleidoscopic behavior, where one structure controllably morphs into another, enabling one material to perform multiple tasks. The findings reveal how reaction-convection processes involving immersed posts produce a distinctive interplay among chemistry, hydrodynamics and fluid-structure interactions.

Author contributions: M.M., O.E.S., and A.C.B. designed research; M.M. performed research; M.M., O.E.S., and A.C.B. analyzed data; and M.M., O.E.S., and A.C.B. wrote the paper.

Reviewers: R.C.H., University of Colorado Boulder; and M.S., Cornell.

The authors declare no competing interest.

Copyright © 2024 the Author(s). Published by PNAS. This open access article is distributed under Creative Commons Attribution-NonCommercial-NoDerivatives License 4.0 (CC BY-NC-ND).

[1]To whom correspondence may be addressed. Email: balazs@pitt.edu.

This article contains supporting information online at https://www.pnas.org/lookup/suppl/doi:10.1073/pnas.2319777121/-/DCSupplemental.

Published March 4, 2024.

Downloaded from https://www.pnas.org by "UNIVERSITY OF PITTSBURGH, FALK LIBRARY /HEALTH SCIENCES" on March 12, 2025 from IP address 136.142.159.80.

which ultimately controls the pattern formation. The singularity of this fingerprint enables the system to act as a chemical sensor, prompting the formation of the characteristic pattern if that chemical is present.

A variety of mechanisms have been used to actuate surface-bound elastic posts, including the application of magnetic (9–12), and electric fields (13–15), light (16–20), elastocapillary (3, 21–23), pneumatics (24–26), and heat (27, 28). Here, we take advantage of the fact that the molecular volume of the reactants for an enzymatic reaction in solution are typically different from the molecular volume of the products generated by the reaction. In solution, the resultant density gradients produce a force, which gives rise to buoyancy-driven, convective flow. In essence, the enzymatic reaction serves as a chemical "pump" that propels flows in fluid-filled chambers (29) and thereby performs mechanical work. The conversion of chemical energy to mechanical action mimics the innate chemo-mechanical transduction in living systems. Similar to the phenomena in biology, chemo-mechanical transduction in these chemically generated, solutal buoyancy–driven flows is an intrinsic, naturally occurring process.

Another distinctive property of enzymatic reactions is that they are highly selective and instigated by only certain reactants. For example, the addition of hydrogen peroxide triggers reactions solely on the catalase-coated posts and thereby generates buoyancy-driven flow centered about these particular structures. As we show, this selectivity drives two posts coated with distinct enzymes to form a dipole-like structure, which forms a fundamental design motif. We then show how to correlate chemistry and fluid flow to form more complex patterns by combining these basic, modular "dipoles."

Notably, there is a wealth of literature connecting reaction–diffusion to the formation of complex patterns in solution. There are, however, few studies on harnessing the coupling between the reaction and convection to actuate posts and control their assembly into complex patterns in solution. In the systems modeled here, reaction-convection leads not only to the spontaneous actuation of the posts, but also to their self-organization into intricate three-dimensional patterns. This mode of actuation and pattern formation is triggered simply by the addition of chemical species to the solution and can ultimately enable the operation of portable microfluidic devices that operate without physical pumps and extraneous power sources.

Acting on deformable materials, the solutal buoyancy mechanism can allow devices such as soft robots to adapt their shape to suit a particular function. This shape changing also facilitates the interaction between robots and compliant systems, such as human bodies.

Theoretical Modeling of Chemically Active Elastic Posts

The surface-anchored catalytic post works as a "chemical pump" that drives the fluid flows toward or away from a post due to solutal buoyancy (29, 30). We consider a fluid-filled rectangular micro-chamber that contains an array of initially vertical elastic posts assembled into a square lattice. Each elastic post is modeled as a linear chain of N beads, described by positions $\mathbf{r}_i$, and interconnected by elastic bonds. The movements of the spherical beads (nodes) are described as

$$\frac{\partial \mathbf{r}_i}{\partial t} = \mathbf{u}(\mathbf{r}_i) \qquad 1 \le i \le N, \qquad [1]$$

where $\mathbf{u}(\mathbf{r})$ is the local fluid velocity at each bead. Each bead in a chain experiences forces due to steric repulsion from the other beads, $\mathbf{F}_s^{nn}$, and from the sidewalls of the channel, $\mathbf{F}_s^{nw}$. The steric repulsion force $\mathbf{F}_s(\mathbf{r}) = -\nabla U(r)$, is computed from the Morse potential (*SI Appendix*). The interbead bonds experience an elastic force, $\mathbf{F}_{el}^{n}$, which is characterized by the stretching (κ_s) and bending (κ_b) moduli and is governed by the linear constitutive relations for a Kirchhoff rod (31). The first bead in each chain is located at a height d from the bottom wall and is anchored to that wall by a spring force at $z = d$. We assume the density of the posts is the same as that of the solvent (ρ_0), so that the posts are neutrally buoyant. To conserve the momentum exchange between the post and the fluid, the forces acting on each of the post beads is balanced by the hydrodynamic drag force $\mathbf{F}^h = -(\mathbf{F}_{el}^{n} + \sum \mathbf{F}_s^{nn} + \sum \mathbf{F}_s^{nw})$.

We explicitly model M reactants and the jth reagent of concentration C_j diffuses with the diffusion constant D_j ($1 \le j \le M$). The chemicals are consumed or produced at the position of the enzyme-coated bead $\mathbf{r}_k$ of the post with a reaction rate given by SK_d where S is the area coated by catalyst. We assume that the catalytic reaction on the post follows the Michaelis–Menten kinetics (32), where the rate of consumption per unit area of the catalytic coverage is given by

$$K_d = \frac{r^{e}_{m,\ post} C_j}{K_M + C_j}. \qquad [2]$$

Here, $r^{e}_{m,post} = k_e[E]$ (in units of $\mathrm{mol\,m^{-2}s^{-1}}$) incorporates the maximum reaction rate per molecule of enzyme, k_e is the reaction rate per molecule, with areal enzyme concentration $[E]$, and K_M (in units of molarity, M) is the Michaelis constant. Both reactants and products diffuse in and are advected by the fluid. The reaction–diffusion–advection equation for the concentration of jth solute, C_j, is

$$\frac{\partial C_j}{\partial t} + (\mathbf{u}\cdot\nabla)C_j = D_j\nabla^2 C_j \pm SK_d \sum_{i=1}^{N} \delta(\mathbf{r}_i). \qquad [3]$$

The "±" sign, represents either production or consumption of the solute (reactants and products).

The enzymatic reactions that occur at the surface of the enzyme-coated posts are coupled to the motion of the surrounding fluid through a solutal buoyancy mechanism. Namely, the enzymes decompose the chemical reactants into products, which can occupy different volumes than the reactants and thus alter the local density of the fluid (4). The change in the local fluid density due to the chemical reaction is given as $\rho = \rho_0\left(1 + \sum_{j=1}^{M} \beta_j C_j\right)$, where ρ_0 is the solvent density and $\beta_j = \frac{1}{\rho_0}\partial\rho/\partial C_j$ is the corresponding solutal expansion coefficient. The density variation in the solution gives rise to a buoyancy force per unit volume given by $\mathbf{F}_b = \mathbf{g}\rho_0 \sum_{j=1}^{M} \beta_j C_j$, where $\mathbf{g}$ represents gravitational acceleration. This buoyancy force drives the spontaneous motion of the fluid and consequently, deforms the immersed post.

The fluid dynamics in the chamber are described by the respective continuity and Navier–Stokes equations [in Bossinesq approximation (33)],

$$\nabla\cdot\mathbf{u} = 0, \qquad [4]$$

$$\frac{\partial \mathbf{u}}{\partial t} + (\mathbf{u}\cdot\nabla)\,\mathbf{u} = -\frac{1}{\rho_0}\nabla p + \nu\,\nabla^2\mathbf{u} + \frac{1}{\rho_0}\left(\mathbf{F}_b + \mathbf{F}^{IB}\right). \qquad [5]$$

Downloaded from https://www.pnas.org by "UNIVERSITY OF PITTSBURGH, FALK LIBRARY /HEALTH SCIENCES" on March 12, 2025 from IP address 136.142.159.80.

Here, $\mathbf{u}$ is the fluid velocity, p is the fluid pressure and ν is the kinematic viscosity. The body forces acting on the fluid have contributions from the solutal buoyancy force, $\mathbf{F}_b$, and the force due to deformations of elastic posts that act on the fluid, $\mathbf{F}^{\mathrm{IB}} = -\sum \mathbf{F}^{\mathrm{h}}$, which is calculated via the immersed boundary method (31) (IBM), providing fluid-structure interactions between the solution and the elastic posts.

We prescribe no-slip boundary conditions at the confining solid walls of the chamber (with equal lateral dimensions $L_x = L_y = L$, and height H) and prohibit the penetration of chemical C_j through the boundaries of the container by specifying

$$\{x, y\} = 0, L \text{ and } z = 0, H: \qquad \mathbf{u} = 0, \qquad \mathbf{n} \cdot \nabla C_j = 0, \qquad [6]$$

where $\mathbf{n}$ is the surface normal.

The set of governing equations (Eqs. **3**–**5**), along with the no-slip boundary conditions for the fluid velocity and no-flux for the chemical concentrations (Eq. **6**), are solved numerically. We use the lattice Boltzmann method for the fluid dynamics, a finite difference method for the reaction–diffusion–advection equations for the reagents, and the IB method for the dynamics of immersed, flexible posts (see *Methods* and *SI Appendix*). The parameters relevant to chemical reactions on the surface of the coated posts are also given in *SI Appendix*, Tables S1 and S2.

Results and Discussion

Patterns Generated with Chemically Distinct Enzymatic Coatings. We consider a fluid-filled chamber of dimensions 4 × 4 × 1 mm with a square array of 9 × 9 vertical elastic posts tethered to the bottom wall (Fig. 1*A*). Five posts located at distinct positions are coated with three different enzymes: one with CAT (catalase) at the center, two coated with AP (acid phosphatase) along the central line in the *x*-direction, and two coated with urease (UR) at diagonal corners. Each enzyme reacts with a separate reagent to generate solutal buoyancy driven fluid flows. The remaining 76 posts are passive; they are not coated with enzymes and just mechanically respond to the flow generated by the active (enzyme-coated) posts. Fig. 1 *C* and *D* show a top view of the square array of elastic posts after adding specific chemicals, in the case of periodic (Fig. 1*C*), and no-slip (Fig. 1*D*) boundary conditions imposed at the horizontal walls of the simulation domain (see Movie S1 in *SI Appendix*). The enzyme-coated posts are shown in red and the passive posts are marked in green. The tips of the passive posts are colored in magenta to indicate the direction of bending. The bending modulus in these simulations is set to $\kappa_b = 0.28\ \mathrm{pN\,mm^2}$. The post configurations remain stable for a few hours until the reactant concentration is depleted and the convective flow is stopped.

In the case where the enzymatic reaction yields lighter products (*Top* panel of Fig. 1*B*), the flow forms vortices that circulate inward near the bottom of the wall (radially directed toward the post). To maintain the continuity of the fluid, this flow moves outward near the top of the post (radially directed away the post). This outward flow exerts a fluid drag that bends the free ends of the nearby passive posts away from the active one. On the other hand, if the post is coated with an enzyme that produces more dense products (*Bottom* panel of Fig. 1*B*), the flow near the top wall is toward the post (inward). As a result, the generated flow drags the free ends of the nearby passive posts to bend in toward the active post.

When hydrogen peroxide (H_2O_2) is added to the chamber, the CAT-coated post decomposes hydrogen peroxide into lighter products, water (H_2O) and oxygen (O_2):

$$2H_2O_2 \xrightarrow{\text{catalase}} 2H_2O + O_2. \qquad [7]$$

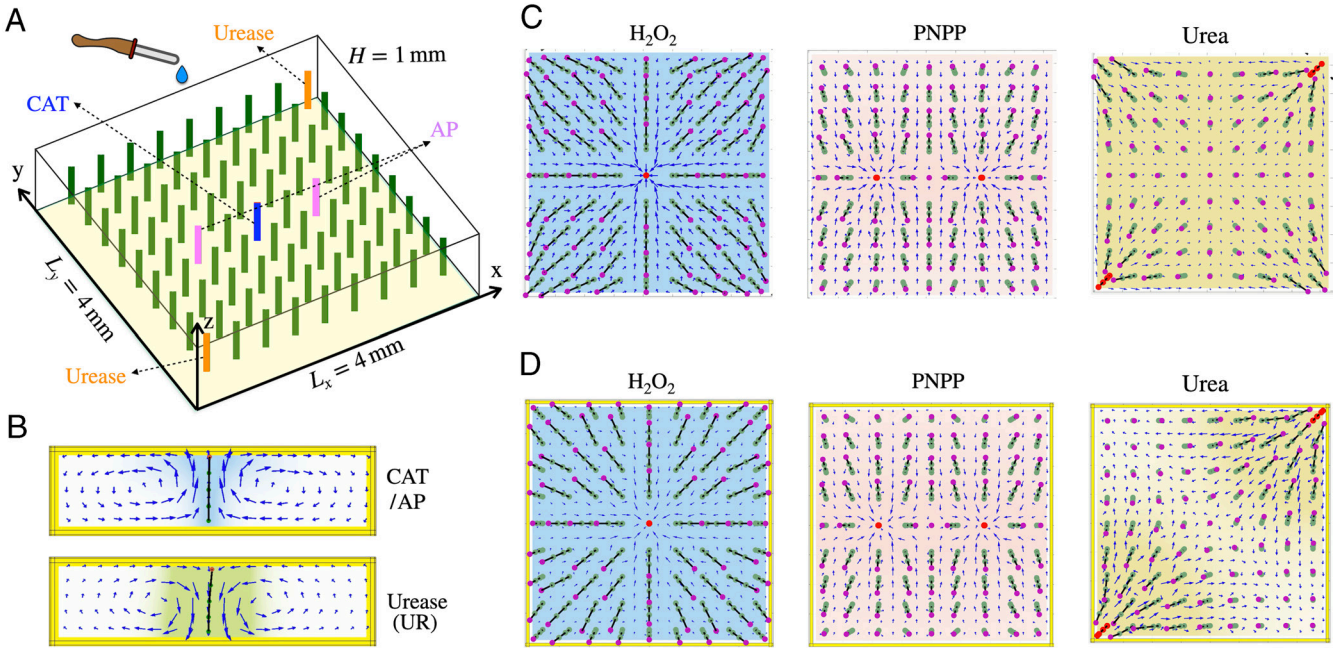


Fig. 1. (*A*) Schematic of a square array of 9 × 9 elastic posts in a fluid-filled rectangular chamber with dimensions 4 × 4 × 1 $\mathrm{mm^3}$ containing five enzyme-coated posts: one with CAT (catalase) in the middle (blue), two with AP (acid phosphatase) along the central line in the *x* direction (pink), and two with urease at corners (orange). By adding appropriate chemicals (hydrogen peroxide, *p*–nitrophenylephosphate and urea) the chemical reaction on the surface of the coated posts drives upward or inward flow that deform the nearby posts. (*B*) Side-view of the flow field generated by an enzyme-coated post that generates inward (CAT or AP) and outward (urease) flow due to the solutal buoyancy effect. (*C* and *D*) Top view of the configuration of a square array of 9 × 9 elastic posts after adding hydrogen peroxide, *p*–nitrophenylephosphate, and urea, for periodic (*C*) and wall (*D*) boundary conditions.

Downloaded from https://www.pnas.org by "UNIVERSITY OF PITTSBURGH, FALK LIBRARY /HEALTH SCIENCES" on March 12, 2025 from IP address 136.142.159.80.

The circulating fluid drives the nearby passive posts to bend radially away from the center (Fig. 1*C*) and the system displays fourfold symmetry. (The solutal expansion coefficient for oxygen is an order of magnitude smaller than the hydrogen peroxide, so we neglect the contribution from oxygen concentration to density (34)).

A different pattern is generated when *p*-nitrophenylphosphate hexahydrate (PNPP) is added to the aqueous solution. The two AP-coated posts in the middle of the domain decompose PNPN into lighter products, p-nitrophenol (PNP) and monosodium phosphate (NaH_2PO_4),

$$\mathrm{PNPP} \xrightarrow{\text{acid phospate}} \mathrm{PNP} + \mathrm{NaH_2PO_4}. \quad [8]$$

A pair of inward circulating vortices forms around each of the active posts, dragging the lighter fluid upward and thus driving the passive posts to bend radially away from each active post. Note that the two posts are collinear along the *x*-direction. The edges of the adjacent vortices meet in a vertical plane that passes between the two posts. To maintain the continuity of the fluid, the flows merging at these central edges move toward the respective active posts. Thus, these central inactive posts are pulled in the opposite lateral direction and consequently remain oriented along the central *y*-axis. As a result, the pattern formed by the elastic posts has a twofold symmetry. (The catalase-coated region of the post remains chemically inactive since the H_2O_2 was not added in this case.)

Finally, when urea ($(NH_2)_2CO$) is added to the chamber, the two enzyme urease (UR)-decorated posts (at the top right and the bottom left corners of the domain) decompose urea into ammonium bicarbonate (NH_4^+ and HCO_3^- ions),

$$\left(\mathrm{NH_2}\right)_2\mathrm{CO} \xrightarrow{\text{urease}} \mathrm{NH_4^+} + \mathrm{HCO_3^-}. \quad [9]$$

In this case, the products are denser than the reactant and the flow generated by the UR-coated posts are outward at the bottom (away from the post) and inward (toward the posts at the top). Hence, the nearby passive posts bend toward the coated ones.

The presence of different types of enzymes and the selectively of the enzymatic reactions enables the production of kaleidoscopic patterns, where one complex geometry can morph into another with the sequentially addition of the appropriate reactants. For example, the patterns in Fig. 1*C* can be converted from one to another (going right to left) with the addition of H_2O_2 and allowing the reaction to proceed until the latter reactant is consumed, and then adding PNPP and, when the PNPP is consumed, adding urea to the solution. As a metaphor, the pattern formation resulting from the sequential addition of reactants resembles the changes in shape made as a kaleidoscope is rotated about its long axis. The steady state of the patterns is reached after about 30 min. This time scale corresponds to an essentially constant average velocity field in the domain and depends on the reaction rate of the active post.

The patterns will appear in the reverse order when PNPP is added first, then H_2O_2 and finally urea. Moreover, the range of patterns formed in this "chemical kaleidoscope" can be augmented by coating passive posts with additional types of different enzymes, as well as adding all the reactants at once.

The imposition of different boundary conditions (BCs) for the H_2O_2 and PNPP cases maintains the morphology and symmetry of the system. The symmetric location of the enzyme-coated posts in the middle of the domain (H_2O_2 and PNPP cases) minimizes the effects of image posts produced by the periodic BCs. Therefore, both BCs preserve fourfold symmetry in systems involving H_2O_2 and twofold symmetry in the cases involving PNPP.

The case involving UR-coated posts, however, does show a dependence on boundary conditions due to the placement of these two posts in the corners. For periodic BCs, chemically active images are introduced in the vicinity of the top left and bottom right corners of the simulation domain. These images, in addition to the two actual active posts located in the top right and bottom left corners (shown in red), operate as four active posts and generate a pattern with fourfold symmetry. In the case with the wall BCs (Fig. 1*D*), the image posts are absent and the resulting pattern displays twofold symmetry (see *SI Appendix*, Fig. S2 for the corresponding post configurations in 5×5 array).

Comparison of Simulations with Semi-Analytical Model. To maintain the continuity of the fluid, the chemically generated vortices must extend to the edges of confining walls. The forces acting on the posts and thus their resultant deflection will depend on the posts' distance from the active, enzyme-coated pillar. To illustrate this behavior and due to symmetry of the system, we focus on a linear array of six posts, where the buoyancy-driven flow is generated by one AP-coated post in the center of the domain when PNPP is added to the solution. The plots in Fig. 2*A* show results from the full simulation, where all the processes described by Eqs. **3**–**5** are taken into account. In particular, Fig. 2 *A, i* provides a side view of the chamber that reveals the deflection of the passive posts neighboring the central, active pillar for the wall BCs; Fig. 2 *A, ii* shows the location of the tip height as a function of time for the same scenario.

The image in Fig. 2 *A, i* reveals that posts multiple units away from the center are still affected by the chemically generated vortices. The plot in Fig. 2 *A, ii*, however, shows that the influence of fluid flow is significantly dampened at post P_5, which lies farthest from the center. The non-monotonic behavior from the simulations for the tip heights (Fig. 2 *A, ii*) reflects the non-linear effects that arise from the combination of chemical reaction, hydrodynamics, and the fluid-structure interactions in the chamber.

We compare the above results with the solutions (Fig. 2*B*), obtained through the elasto-hydrodynamic theory presented in *Methods* where the flow produced by the central AP-coated post is approximated as that produced by five distinct point forces at the location of the beads and directed along the positive *z*-axis (For a UR-coated post the direction of the point forces is along the negative *z*-axis; see *SI Appendix*, Fig. S5). Fig. 2 *B, i* and *ii* show the same trends as the corresponding plots in Fig. 2*A*. The forces acting on the posts decay with distance for central active unit. The results in Fig. 2 *B, ii* from the analytical model, however, do not show the presence of minima in curves. The minima arise from non-linear interactions that are not included in the simplified analytical description. Nonetheless, the general agreement between the results from the two models supports the predictions from the more complete description provided by the simulations.

Varying Chamber Height and Introduction of Defect. Changing the space around a given post, by either changing the dimensions of the fluidic chamber or introducing defects in the array, plays an important role in controlling the mechanical response and pattern formation in the system. To illustrate the effect of varying the chamber dimensions, we fix the post length *L* and perform simulations for different chamber heights *H*. In the case for one CAT-coated post at the center of the 9×9 array, increasing *H* from 1 mm to 2 mm alters the orientation of the passive posts from radially bending away from the active post to radially bending toward this post (Fig. 3). Increasing the height of the chamber leads to position-dependent changes in the flow direction and the speed within the vortex formed between the top and bottom walls.

Downloaded from https://www.pnas.org by "UNIVERSITY OF PITTSBURGH, FALK LIBRARY /HEALTH SCIENCES" on March 12, 2025 from IP address 136.142.159.80.

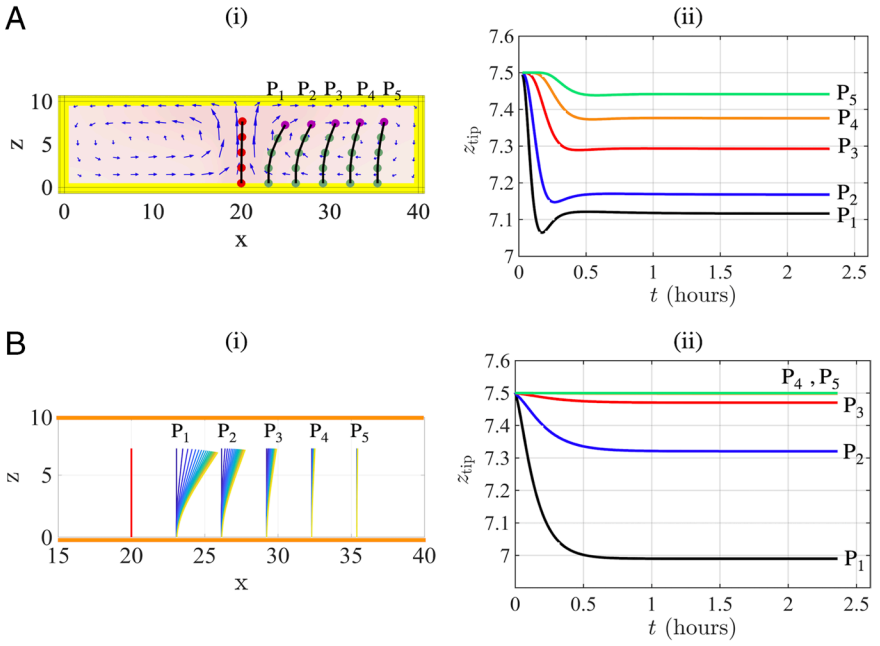


Fig. 2. Comparison of the motion of five passive posts in the presence of one AP-coated post at the center as obtained using the computational simulation (*A*) and elastohydrodynamic theory (*B*). The height of the chamber is $10\Delta x$ and the length of the posts is $L = 7.5\Delta x$ where $\Delta x = 0.1$ mm is the lattice Boltzmann unit. In the right, we plot tip heights of the posts as a function of time.

Hence, a change in H causes a post of fixed length to experience different regions of the vortex. Similarly, for a change in L at fixed H, the posts of various lengths experience different flow profiles and drag forces. Consequently, the ratio L/H is pivotal in controlling the formation of the patterns (see Movie S2 in *SI Appendix*).

Defects are introduced by removing some of the passive posts from the array and thereby modifying the spatial and temporal effects imposed on each remaining post. To demonstrate the significant influence of defects, we consider a square array of 13×13 elastic posts, with one CAT-coated pillar in the center and remove nine posts from the four different quadrants of the simulation box. (Here, a defect refers to the region where all nine posts have been removed.) Fig. 4 shows the respective patterns with defects in one, two, three, or all the four quadrants. In each quadrant, the posts bend away from the central pusher and toward the vacancies left by the removed posts.

When nine posts are removed just from the first quadrant (Q1), we observe distinct spatiotemporal behavior: two of the posts undergo greater bending and begin to oscillate (*SI Appendix*, Fig. S3 and Movie S3). The behavior is robust and occurs when this single defect is located in any of the other quadrants (Q2, Q3, or Q4). As more defects are introduced, into the lattice (Fig. 4 *B–D*), any initial oscillations in the system are suppressed with time. This behavior indicates that defects "communicate" and experience effects from other quadrants.

To demonstrate the above point, we plot two lateral components of the velocity field (parallel to $x - y$ plane) u_x and u_y as a function of height z for a point at the center of the defect in Q1. The flow profile with just one defect (Fig. 4*A*) reveals that u_x and u_y are equal in value due to the symmetry of the fluid flow with respect to diagonal plane, $y = x$. When we measure u_x and u_y at the same point in Q1 in the presence of a defect in Q2, the velocities in the x and y directions no longer coincide with each other, showing that the configuration of passive posts in the second quadrant (Q2) influences the flow pattern that now affects the behavior of the defect (in Q1). Notably, the values of and u_x and u_y at the extrema (maximum and minimum) are shifted from their original values with the defect in Q2. As defects are introduced into Q3 and Q4, the values of u_x and u_y come closer together, until they again approximately coincide with each other and display essentially the same values as in Fig. 4*A*.

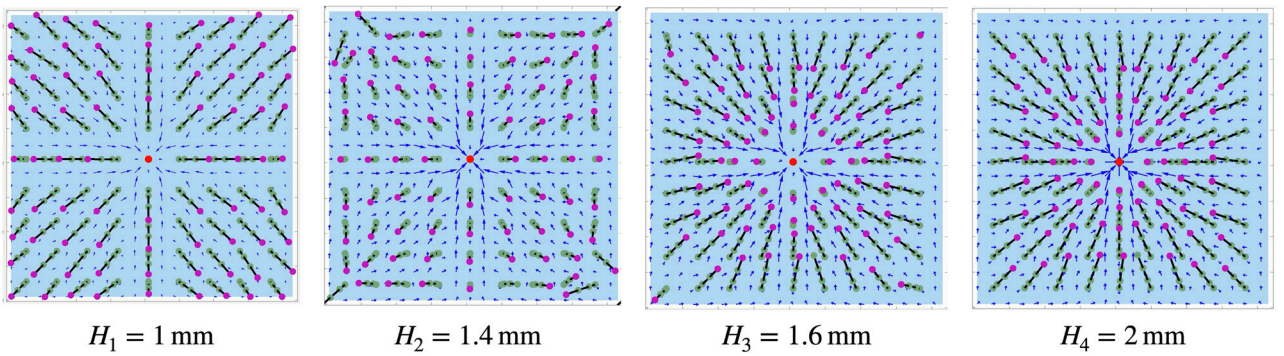


Fig. 3. Top view of the arrangements of an square array of 9×9 elastic posts with one CAT-coated post in the middle, for different heights of the wall: $H_1 = 1$ mm, $H_2 = 1.4$ mm, $H_3 = 1.6$ mm, and $H_4 = 2$ mm for periodic BCs.

Downloaded from https://www.pnas.org by "UNIVERSITY OF PITTSBURGH, FALK LIBRARY /HEALTH SCIENCES" on March 12, 2025 from IP address 136.142.159.80.

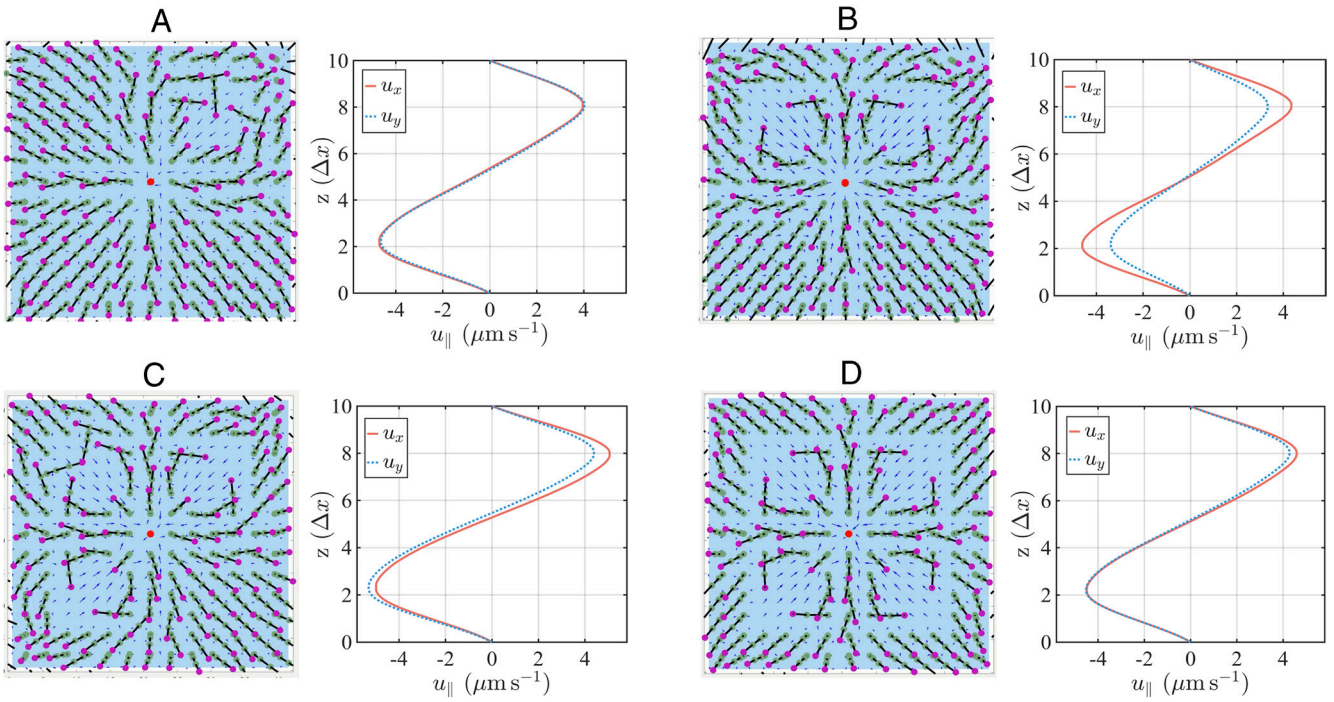


Fig. 4. Top view of the arrangements of a square array of 13 × 13 elastic posts with one CAT-coated post in the middle, with defects (nine removed posts) in each of the four quadrant of the simulation box for periodic BCs. In the right, we plot the lateral velocity profiles ($u_\parallel$ is either u_x or u_y) at the center of the defects, for defects in one (*A*), two (*B*), three (*C*), and four (*D*) quadrants.

The flow pattern with just one defect (in Q1) results from a unique interplay among chemistry, hydrodynamics and fluid-structure interactions and leads to a unique instability in the system. Fig. 4 provides some insight to the origin of the distinct oscillatory behavior. While the circulating convective flow reaches the edges of the confining walls in all cases, it is evident that the void and free volume around the defect are greatest in Fig. 4*A*. The greater free volume allows the posts to sample a larger number of configurations; the encircled posts in *SI Appendix*, Fig. S3 have sufficient space to undergo oscillatory behavior.

In Fig. 4 *B–D*, the presence of vacancies does increase the range of motion of the remaining posts and decreases the amount of steric interactions in the domain. Conversely, the confined fluid has a finite volume and hence can only perform a set amount of mechanical work as it bends a post. When the fluid and generated force is partitioned among more quadrants, the magnitude of force exerted by the flow is reduced as a function of the distance from the active post (Fig. 2). This reduction in the forces in turn limits the bending of these posts and their potential for mechanical oscillations. Finally, in Fig. 4*D*, the four vortices control the pattern formation, as the remaining posts in each quadrant follow the contour lines generated by the circulating solution and the systems form the symmetric pattern.

The systems described above captures a particular combination of chemistry, flow and fluid-structure interactions. Nonetheless, the behavior illustrates a scenario that can occur in other systems where reduction in the magnitude of the generated force reduces the size of the affected domain. The latter shrinking in available free volume introduces new steric interactions that can prevent oscillatory behavior.

Illustration of Oscillatory Behavior. Fig. 5 illustrates the salient dynamic behavior of posts when they do display oscillatory behavior. The bending stiffness of the posts plays an important role in promoting oscillations in the system. In the previous simulations, we set the bending modulus to $\kappa_b = 0.28$ pNmm^2; we now take the posts to be more flexible and fix the bending modulus at $\kappa_b = 0.076$ pNmm^2 (reduced the bending modulus by a factor of 3.7). For the latter modulus, we consider a square array of 5×5 posts, where the buoyancy-driven flow is generated by one CAT-coated post located in the center of the domain and we have imposed wall BCs (see *SI Appendix*, Fig. S2 for the patterns with stiffer posts, i.e., when $\kappa_b = 0.28$ pNmm^2).

The oscillations in this system involve the circulatory motion of the posts, which can be readily seen by focusing on the tip site (Fig. 5 *B–D*). Due to the symmetry of the system, we can analyze the system's behavior by focusing on three representative posts located in the first quadrant. Initially, posts P_1 and P_3 start to oscillate in-phase with similar amplitude (Fig. 5 *B* and *D*). The posts are sufficiently flexible that they can bend to the degree that their tips almost touch the bottom of the chamber. An opposing flow at this bottom wall (see velocity profiles in Fig. 4) drives the posts to move in a circulatory orbit within the confined domain (*SI Appendix*, Fig. S6).

With time, the motion of post P_2 (and also the two closest posts to P_2, i.e. P_4 and P_5) circulates in a smaller orbit and oscillates with reduced amplitude, as shown in Fig. 5*C*. For the set of parameters used in the simulations, the period of oscillations is $T \sim 15$min (see Movie S4 and *SI Appendix* for the parameters characterizing the catalytic reaction rate, diffusivity, etc.).

The above discussion is meant to simply illustrate different types of the post dynamics appearing in the system, which may include the posts' oscillatory motion. We will describe this non-linear dynamic behavior more fully in a subsequent paper.

Formulation of Simple Design Rules. Combining the effects of two (or more) different enzymatic coatings creates a means of fashioning the self-organization of the posts and modifying the system's functionality without the need to fabricate a new device

Downloaded from https://www.pnas.org by "UNIVERSITY OF PITTSBURGH, FALK LIBRARY /HEALTH SCIENCES" on March 12, 2025 from IP address 136.142.159.80.

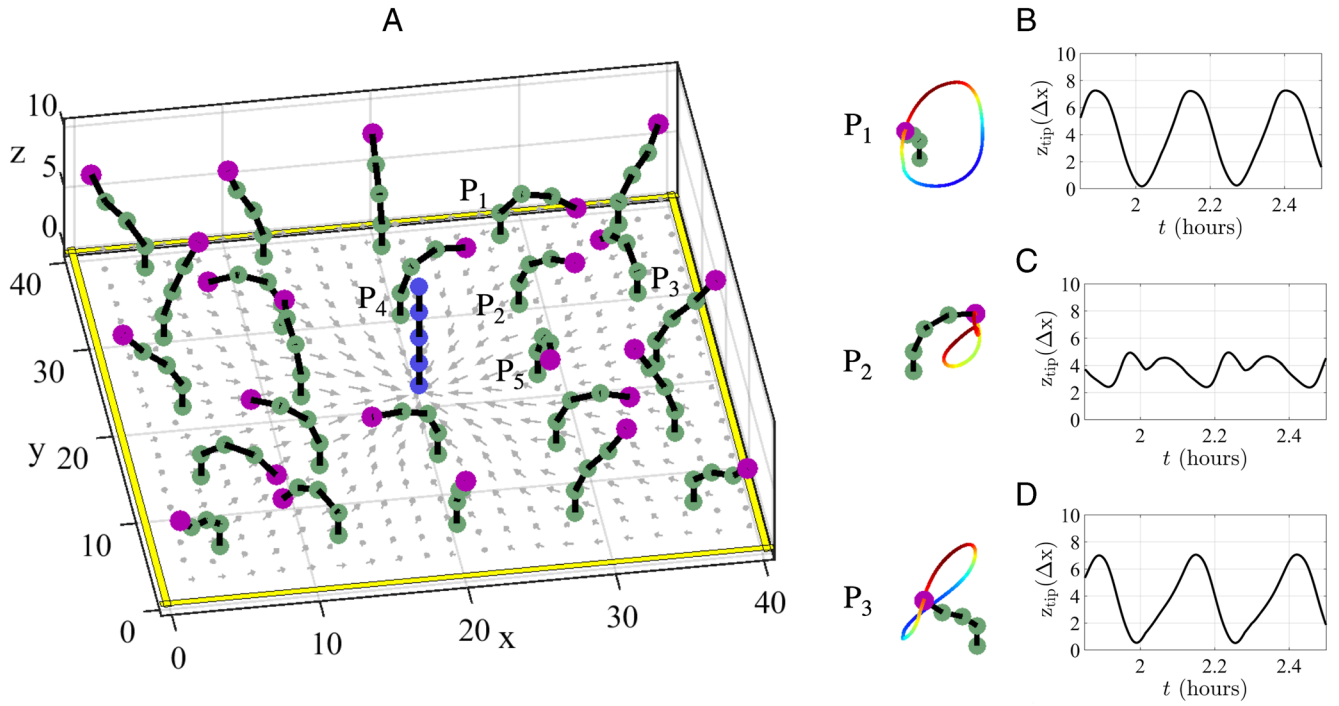


Fig. 5. (*A*) Top view of the time dependent motion of a square array of 5 × 5 elastic posts with one CAT-coated post in the middle for wall boundary conditions. The posts are more flexible with bending modulus of $\kappa_b = 0.076\ \mathrm{pN\,mm^2}$. (*B–D*): Trajectories and time-dependent motion of posts tips P_1, P_2, and P_3 in the first quadrant. The oscillation amplitude of the corner posts (P_1 and P_3) is the same, but larger (about three times) than the posts near the CAT-coated post. They undergo oscillation with period of $T \sim 15$ min.

for each specified task. For example, for applications involving microfluidics, the posts can act as walls that form transient channels to guide the fluid flow and immersed objects (such as microparticles or bacteria) to particular locations in the chamber. With the addition of appropriate reactants, the layout of the walls could be dynamically reconfigured to suit new functions. These patterns can be maintained for hours and even much longer if fresh reactants are added to the solution. The challenge is establishing design rules for achieving the desired patterns within the flexible posts through a combination of chemistry, directed flow, and location of the coated posts.

As a step in formulating this design process, we initially focus on a system that encompasses just one specific type of enzyme. In Fig. 6*A*, we employ AP-coated posts (four, five, eight, and nine, going from left to right) within a square array that encompasses 81 units. The AP-coated posts (shown in blue) generate an inward flow, which effectively "pushes" the passive posts away from the active ones. Keeping the location of the active posts fixed, we replace the AP-coated posts with UR-coated ones (shown in red in Fig. 6*B*). The latter posts generate outward flow, which effectively "pulls" the passive units toward the active species. Fig. 6 reveals the selectivity of the catalysts, where the generated patterns depend on the kind of enzyme at a specified position (see Movie S5 in *SI Appendix*). The figure also reveals the cooperative behavior between posts coated with the same enzyme.

We use the above information to analyze pattern formation in more complex systems, which involve the simultaneous presence of both the reactants. In the latter case, we consider the pair of a "pusher" and "puller" forming an effective dipole (Fig. 7*i*), since the unit at one end "repels" the passive posts and the unit at the other end "attracts" these posts. To formulate effective design rules, we consider this dipole as the modular design element. Fig. 7*ii* shows the flow lines (on the bottom surface) obtained from the simulation for such a single dipole.

The results in Fig. 8 are obtained by simultaneously adding both the appropriate reactants to the system. The schematics on the right pinpoint the locations of the pushers and pullers for the corresponding results on the left. The latter patterns reveal how various combinations of modular dipole units lead to complex patterns. We fix the geometry of the system in Fig. 8*A* and exchange the relative location of the red and blue posts to obtain the simulation results in Fig. 8*B*; the positions of the passive posts remain fixed. This exchange corresponds to reversing the orientation of the modular dipoles in the system. Indeed, the pattern in Fig. 8 *A, i* shows that all the posts are pointed away from the center of the box, in the opposite direction as in Fig. 8 *B, i*. Hence, the relative orientation of the dipoles provides another design component.

Fig. 8 *A, i* shows four symmetric repetitions of the image of a single dipole, where the axis of each dipole is aligned along a diagonal line in the box. Outward flow generated by each of the four red posts "pulls" other posts toward each corner. The central blue post generates inward flow, which pushes tips uniformly away from the center, reinforcing the bending of the tips toward the corners. In this scenario, the enzyme-coated sites act in a cooperative manner to generate the pattern seen in Fig. 8 *A, i* two enzymes. We place one AP-coated post at the center and four and eight UR-coated posts at symmetric positions in the square domain in panel (*A*). In panel (*B*), we exchange the position of AP and UR-coated posts.

The exchange of the relative location of the red and blue posts in Fig. 8 *A, i* leads to the results shown in Fig. 8 *A, ii*. As can be seen, the combined effect of the four blue posts dictates the pattern within each of the four quadrants. The addition of the red central pillar does not have a significant effect on the observed pattern since passive posts were driven toward the center by the "repulsion" from the peripheral, blue pushers. The red puller at the center reinforces the latter behavior. This cooperative push–pull relationship now

Downloaded from https://www.pnas.org by "UNIVERSITY OF PITTSBURGH, FALK LIBRARY /HEALTH SCIENCES" on March 12, 2025 from IP address 136.142.159.80.

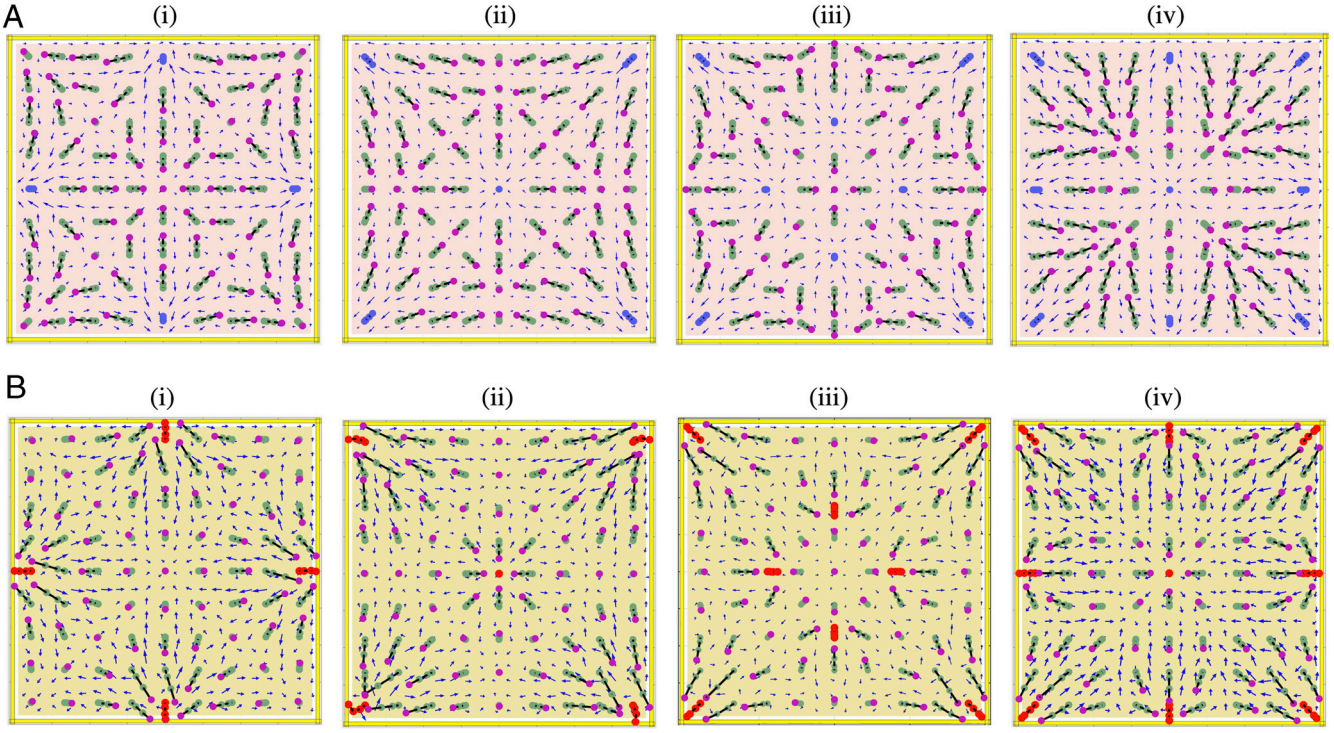


Fig. 6. Top view of the final arrangements of a square array of 9 × 9 elastic posts, with AP, panel (*A*), and UR, panel (*B*), coated posts when we add PNPP and urea, respectively. The coated posts are colored with blue (AP) and red (UR). All of the figures are for wall BCs.

drives all the posts to point toward the red pillar in the center (Fig. 8 *B, i*).

In Fig. 8 *A, ii*, the dipoles are oriented parallel to the *x* and *y* axes. The cooperative effects of the pullers at the rectilinear edges drive the posts along the *x* and *y* axes to be oriented away from the center and toward the edges of the box (to the center of an edge). The introduction of the blue pusher at the center of the array does influence this pattern. Namely, due to the square symmetry of the system, posts in the center of each quadrant are now equally pushed away from planes that cut laterally and vertically through the center. To accommodate these symmetric forces, centrally located posts in each quadrant assemble into a curved shape about orthogonal axes, so that the figure resembles a four-leaf clover. Put in another way, the addition of the central blue post introduces a new radially repulsive force, which now pushes posts that were relatively unaffected in Fig. 6 *B, i* to extend away from the middle of the square. In this location, the blue and red posts introduce opposing forces, which do modify the pattern relative to the situation without a post in the center.

Fig. 8 *A, iii* and *B, iii* involve not only an exchange in the position of the pushes and pullers, but also turning some of the passive posts into new active ones. Fig. 8 *A, iii* contains remnants of Fig. 8 *A, ii*, but the addition of the four red pullers removes the pinching of leaves toward the respective axes and thus changes the clover leaf pattern to one that resembles a cross. Similarly, Fig. 8 *B, iii* contains remnants of Fig. 8 *B, ii*, where four blue posts are located in the same position in both cases; the comparison of these two figures shows how the addition of specific active post at symmetric and strategic locations enables the designer to controllably augment the richness of the self-organized pattern.

As more passive posts are replaced by active ones and the number of active units is thereby increased, their influence more directly affects the neighboring non-coated pillars. Namely, extensive fluid flow is broken down into smaller streams that primarily exert local influence. The behavior is useful for creating patterns; the local bending can be predicted and controlled with the knowledge that the reaction generates inward or outward flow.

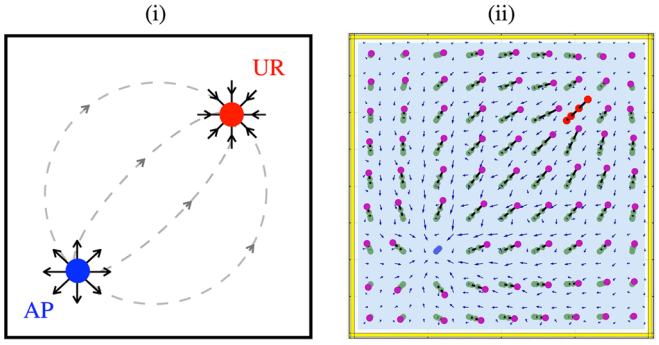


Fig. 7. (*i*) Schematic of a "puller-pusher" pattern as a result of two kinds of enzyme-coated posts: pushers (AP) in blue and puller (UR) in red. (*ii*) The corresponding configuration generated in a square array of 8 × 8 posts when we add two chemicals that react with the two enzyme-coated posts.

Distinctiveness of the Patterns. The above examples illustrate the wealth of designs that can be formed with just two different types of enzyme coatings. Based on these findings, we argue that for a given choice in the location of the active posts within the array and chemical identity of enzymes, the system forms a unique surface pattern. (Here, we assume that the height of the chamber, flexibly of the posts and temperature is held fixed.) Each set of such choices provides a distinct "fingerprint," which reflects the specific system's parameters.

Consider the simplest case: the only parameter that is changed is the location of a single active post in the array. In the new location, the active post encounters new neighbors and thus, experiences new fluid-structure interactions, which affect the resultant

Downloaded from https://www.pnas.org by "UNIVERSITY OF PITTSBURGH, FALK LIBRARY /HEALTH SCIENCES" on March 12, 2025 from IP address 136.142.159.80.

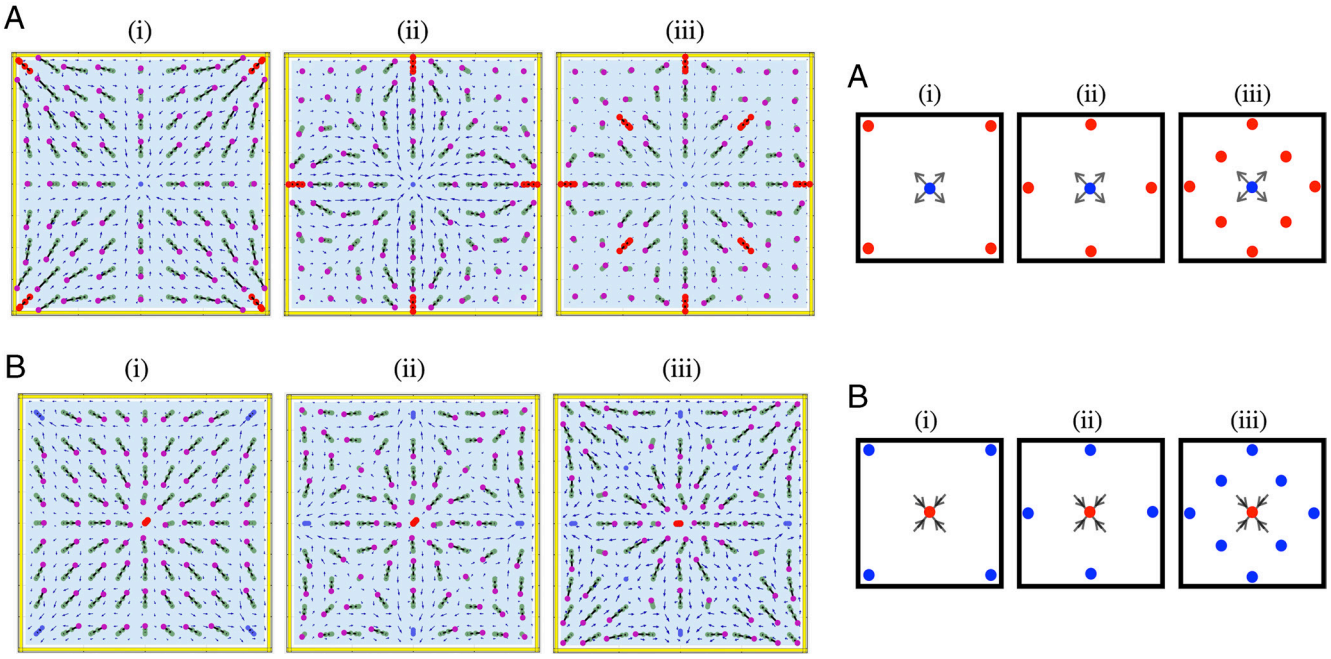


Fig. 8. (*A*) Top view of the final arrangements of a square array of 9 × 9 elastic posts, with posts coated by two enzymes (AP: blue posts, urease: red posts). Both reactants that respectively trigger the two enzymes reactions are present in the solution. One AP-coated post is positioned at the center, and four or eight UR-coated posts are placed in symmetric positions in the square, as displayed in the schematic at the right. (*B*) The simulation results when the positions of the AP and UR-coated posts are switched (as shown in the schematic on the right).

flow profiles (as well as non-linear dynamics of the entire system). Hence, shifting the location of just one active post yields a new fingerprint.

Now consider the case where the position of the posts is held fixed (as are all the other parameters), but a different enzymatic reaction is used to actuate the array. The solutal buoyancy force per unit volume acting on the system is given by $\mathbf{F}_b = \mathbf{g}\rho_0 \sum_j \beta_j C_j$, where the sum is over all the chemical species j. Each enzymatic reaction involves a specific set of reactants and products and hence, the sum $\sum_j \beta_j C_j$ is distinct for each reaction. (The latter statement is valid unless there exits the exceptional, fortuitous case where the sums are mathematically identical in magnitude for two different cases; however, even in the rare case where these magnitudes are identical, the specific sign of β_j is critical since it dictates whether the flow is inward or outward and hence affects the global flow.)

The expression for $\mathbf{F}_b$ also depends on the values of C_j, the concentration of each component. With all other parameters held fixed, variations in C_j alone will impact the pattern formation, since this parameter affects the value of K_d (Eq. **2**) and thus the reaction rate SK_d. Increases in reaction rate lead to increases in the fluid velocity (35), which increases the force acting on the post and thereby influences the shape assumed by the entire structure.

As the size of the array and chemical choices are increased, the number of possible combinations of parameters becomes dramatically large and further point to the potential for the uniqueness of the fingerprint for a specific system.

Design of Complex Patterns. The concepts now allow us to design distinct patterns with specific structural motifs. To fashion an example with a hierarchical configuration, we increase the density of the posts in the array from 81 to 169. We a prior pick a shape we aim to create and then use our design strategies to form that pattern. In particular, we aimed to create an arrangement that encompasses the basic components of a "mandala" figure: a square containing "four gates" and a circle with a center point. We achieved this design by placing five AP-coated post at the appropriate locations, as shown in Fig. 9. Collinear, active posts are symmetrically placed at rectilinear positions and push the posts radially away from these corners. Due to the square symmetry in the system, some of these bent posts form lines that constitute the sides of a square, one of the needed elements for the mandala (Note that the latter cooperative behavior leads to the formation of both an inner square and the outer square at the boundaries of the simulation box).

Having learned from the example in Fig. 8, we recognize that placing a coated post in the center ensures the radial symmetry needed to form a circle about the central point. The mutual repulsion of the corner and central sites leads to the formation of four symmetric ovals at the center sample. The ovals constitute gates because they enable fluid flow into and out of this corralled region.

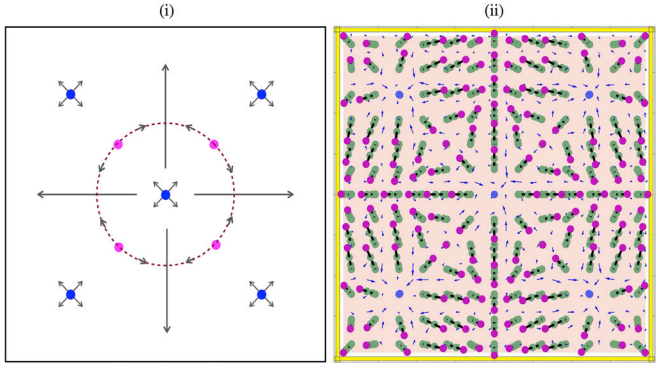


Fig. 9. (*i*) Schematic of the target pattern created in the right figure; blue dots are the position of active posts, and the pink dots are the stagnation points. (*ii*) Top view of a square array of 13 × 13 elastic posts. When PNPP is added to the solution, the AP-coated posts react and create a mandala-like pattern.

Downloaded from https://www.pnas.org by "UNIVERSITY OF PITTSBURGH, FALK LIBRARY /HEALTH SCIENCES" on March 12, 2025 from IP address 136.142.159.80.

Conclusions

In solution, numerous chemical reactions generate gradients in the density of the fluid as reactants are converted to the products of the reaction. These density gradients give rise to a solutal buoyancy force, which leads to convection in the bulk fluid. The convective flow can in turn exert a force on submerged elastic materials that morph the material's shape. Hence, there is a direct connection among the chemistry of the reaction, the flow patterns generated by convection and the shape of the soft materials. Here, we show how this coupling of reaction and convection yields a design tool for patterning soft active matter.

We focused on enzymatic reactions that drive inward or outward circulating flow that acts on an array of passive and active anchored posts, which were coated with these different types of enzymes. Taking advantage of the specificity of enzymatic reactions (which are triggered by only certain reactants), we proposed that each sample of chosen parameters provided a distinct fingerprint that characterizes that specific system.

Due to such distinctive features, these responsive systems can act as sensors, with the design reflecting the presence or absence of chemicals in the solution; if present, a well-defined pattern will emerge that does not appear in the absence of that chemical species. Moreover, the pattern can reflect the concentration, C_j, of each species present in the solution. Conceptually, the system is similar to an electronic nose (36) where a volatile compound interacts with an array of sensors and generates patterns of signals. The latter data that is analyzed by a pattern recognition system and with the aid of machine learning, a specific pattern is associated with a particular compound. Hence, the specific design generated through the interaction between the compound and the sensors reveals its chemical identity. An advantage of the proposed systems is that the generated patterns are sufficiently large (micron to millimeter scale) that the images can be readily captured through microscopy or direct photography, providing a facile mechanism for recording the data needed for the subsequent pattern recognition tools. Additionally, the chemically generated fluid flow drives the reagents over the sensors, alleviating the need for extraneous pumps to propel the fluid over the sensors.

The specificity of enzymatic reactions also allowed us to design chemical kaleidoscopes, which encompass a number of different active posts at fixed locations. The addition of a certain reactant causes the posts to form a particular pattern, which can be morphed into another distinct design with the addition of another reactant. The number of kaleidoscopic patterns in a system can be augmented by increasing the number of distinct active posts. Since the observed patterns depend on chamber height, H, then dynamically altering H, can also lead to kaleidoscopic behavior.

The examples shown throughout this paper form a "language" for forming specific patterns. Each of the distinct components (i.e., the square walls, central circles, symmetric ovals) constitutes a basic element in this "pattern language" (37). Given this language, the designer can ultimately learn how to utilize the placement and types of enzymes to form these basic elements, and then how to combine the basic elements into particular motifs, which then can be used to form more intricate, hierarchical structures.

For posts with a given coating, length, and flexibility, different patterns could be induced by altering the geometry of the fluid-filled containers since the walls of the chamber strongly influence the convective velocities in the micro-chamber (8). Additional controlled morphing of the patterns could be induced with cascade reactions, where the product of one reaction is the reactant for the next.

To facilitate future experimental studies, we specify physical values that correspond to numbers used in the simulation. The magnitude of the fluid flow is characterized by the ratio of solutal to viscous forces, expressed by the dimensionless Grashof number, $\mathrm{Gr} = \frac{g\beta\Delta C H^3}{\nu^2}$, where β is the solutal expansion coefficient, ΔC is the chemical variations in the domain, and ν is the kinematic viscosity of the fluid and H is the height of the chamber (*SI Appendix*). The typical Grashof number in our system is about 10^2. The velocity of buoyancy-driven flow depends on a specific set of reactants (β values): higher solutal expansion coefficients will produce faster induced flows. The elastic properties of the posts are characterized by the ratio of the restoring elastic force to viscous force, $\tilde{\eta}^{-1} = \frac{B/L^2}{C_N \dot{\gamma} L^2}$, where L is the length of the post, B is the flexural rigidity, C_N is the transverse drag coefficient and $\dot{\gamma}$ is the shear rate (*Methods*). For a post with $B \sim 0.07$ pNmm^2, in a flow with shear rate $\gamma \sim 10^3 \mathrm{s}^{-1}$ and $C_N \sim 1.4\pi\eta$, we obtain the value of $\sim 5 \times 10^{-2}$ for this dimensionless ratio.

In addition to the facilitating the formation of chemical sensors, the ability to control the dynamics of the fluid with engineered micro-patterned posts is valuable for devising new applications for labs-on-chips (38, 39) and enabling the facile reconfiguration of the walls in microfluidic devices. While just touched on here, in future studies, we will investigate the rich dynamic behavior and oscillatory patterns that can emerge when the posts are sufficiently flexible.

Methods

The continuity and Navier–Stokes equations are solved using the lattice Boltzmann method (40) (LBM) with a single relaxation time D3Q19 scheme (41). A finite difference approach with a forward-time central-space (FTCS) scheme is used to solve the advection–reaction–diffusion of chemicals. The immersed boundary (IB) approach is used to capture the fluid-structure interactions between the elastic posts and fluid. In the IB model, each node of elastic post is modeled by a sphere with effective hydrodynamics radius a that experiences fluid drag, characterized by the mobility $\mathrm{M} = (6\pi\eta a)^{-1}$. The forces $\mathbf{F}_{\mathrm{el}}$ exerted by the nodes of the elastic post on the fluid, which are calculated using the IB method, provide zero fluid velocities at the discretization nodes of the elastic post. Therefore, the IB approach approximates no-slip conditions for the fluid velocities at the boundary nodes, as well as no fluid permeation through the nodes of the posts. We keep the post's diameter and the elastic moduli constant and vary the type, position of the enzyme-coated posts and chemical reagents to analyze the patterns formed in the micro-chamber.

The size of computational domain is $40\Delta x \times 40\Delta x \times 10\Delta x$ where the lattice Boltzmann unit Δx is 100 μm. The time step of the simulation is $\Delta t = 1.67 \times 10^{-3}$ s. In the IB approach, each of the discretized nodes of the post is treated as a sphere with radius $a \approx 1.3\Delta x$. Consequently, the effective diameter of a single post is $2a = 260$ μm. Each post is discretized into $N = 5$ beads with the equilibrium distance between the beads as $ds = 1.75\Delta x$. Moreover, we place the first bead at distance $0.5\Delta x$ from the wall, so that the total length of the post is $L = 7.5\Delta x$. For a square array of 9×9 posts, the inter-cilium spacing is $\delta = 40/9\Delta x$. In the majority of our simulations we assume that the elasticity of the flexible posts can be characterized by a Young modulus on the order of 70 MPas.

For the semi-analytical calculation, we couple elasticity theory and overdamped viscous hydrodynamics (42–50) to obtain the time-dependent motion of the posts, where the external background flow is taken from the flow induced by one active enzyme-coated post at the center of the domain. We consider a slender inextensible elastic post of length L, with circular cross-section of radius a at its midpoint, where the centerline is identified by $\mathbf{X}(s, t)$ which is a function of both time, t and arc length $0 \le s \le L$. The end $s = 0$ is clamped against a no-slip wall, and $s = L$ is free. The surrounding fluid has a viscosity η, and the flow is assumed to be sufficiently slow that the Reynolds number is small. At any local point along the post, the instantaneous force balance satisfies

Downloaded from https://www.pnas.org by "UNIVERSITY OF PITTSBURGH, FALK LIBRARY /HEALTH SCIENCES" on March 12, 2025 from IP address 136.142.159.80.

$$\mathbf{f}^e + \mathbf{f}^h = 0, \qquad [10]$$

where $\mathbf{f}^h$ is the hydrodynamic force per unit length, and $\mathbf{f}^e$ is the elastic force per unit length

$$\mathbf{f}^e = -B\mathbf{X}_{ssss} + (T\mathbf{X}_s)_s, \qquad [11]$$

where B is flexural rigidity, T is axial tension (Lagrange multiplier) that ensures the condition of inextensibility, and subscript s denotes the partial derivative with respect to s. We take advantage of small aspect ratio of the post ($\varepsilon = a/L << 1$) and use the resistive force theory (RFT) (51) that linearly relates $\mathbf{f}^h$ to the instantaneous relative velocity of the post along the centerline such that:

$$\mathbf{X}_t - \mathbf{U}^\infty = -M_\circ[\mathbf{I} + (\xi - 1)\mathbf{X}_s\mathbf{X}_s]\cdot\mathbf{f}^h, \qquad [12]$$

where $M_\circ = \frac{\ln(\varepsilon^{-2}\mathrm{e})}{8\pi\eta}$ is the perpendicular mobility of the post, ξ is the ratio between parallel to perpendicular mobility (52) ($\xi = 2$ for $\varepsilon \to 0$), $\mathbf{I}$ is the identity tensor, and $\mathbf{U}^\infty$ is the background flow. If we rescale the length by L, time with inverse of shear rate, $\dot{\gamma}^{-1}$, and tension with $T = \frac{B}{L^2}$, we get (53, 54):

$$\tilde{\eta}(\mathbf{X}_t - \mathbf{U}^\infty) = -\mathbf{X}_{ssss} - (\mathbf{X}_{ssss}\cdot\mathbf{X}_s)\mathbf{X}_s + 2T_s\mathbf{X}_s + T\mathbf{X}_{ss}, \qquad [13]$$

where $\tilde{\eta} = \frac{\dot{\gamma}L^4}{M_\circ B}$ is the ratio between viscous to elastic force. The limit $\tilde{\eta} \to 0$ and ∞ corresponds to a rigid rod and a flexible thread (55), respectively. Taking the derivative of both side of the equation with respect to s and then taking dot product of both side by $\mathbf{X}_s$ gives us the other scalar equation:

$$\begin{aligned} &7\mathbf{X}_{sss}\cdot\mathbf{X}_{ss} + 6\mathbf{X}_{sss}\cdot\mathbf{X}_{sss} + 2T_{ss} - T\mathbf{X}_{ss}\cdot\mathbf{X}_{ss} \\ &+ \tilde{\eta}\mathbf{U}^\infty_s\cdot\mathbf{X}_s - \alpha(\mathrm{J}_{N,1} - \mathbf{X}_s\cdot\mathbf{X}_s) = 0, \end{aligned} \qquad [14]$$

where α is a penalty term (we take $\alpha = 10^4$), and $\mathrm{J}_{N,1}$ is $N \times 1$ array of all "1"s, when we divide the post centerline to N grid points. The resulting system of linear equation is solved numerically to obtain the tension and time dependent position of the elastic post. Assuming a constant shear rate of order $\dot{\gamma} \sim 10^{-3}\mathrm{s}^{-1}$, aspect ratio of $\varepsilon \sim 0.1$, $L = 0.75$ mm, and flexural rigidity $\tilde{\eta} \sim 20\,B \sim 0.07$ Nmm^2, we obtain ~ 20 for our system.

To obtain the motion of the post, we assume that a single passive post is placed in the flow generated by the enzyme-coated post. This flow in general is time dependent, due to advection and diffusion of the chemicals, but in the limit of small Reynolds number ($\mathrm{Re} = \rho\mathrm{LU}/\eta \sim 10^{-3}$), we can approximate the background flow as the steady flow generated by a collection of point forces located between two parallel plates [see Liron and Mochon (56)]. We use the Stokes flow field due to five point forces placed along a vertical line at different heights and all having orientations along the positive (negative) $\hat{\boldsymbol{z}}$ direction.

The net effect of the point forces approximates the action of buoyancy forces produced by the less-dense chemicals catalyzed on the active post. The resulting flow mimics the simulation results where fluid motion is generated by one active post coated with CAT (UR) enzyme (*SI Appendix*, Fig. S5). We insert the background velocity field, $\mathbf{U}^\infty$, in Eqs. **13** and **14** to obtain solutions for the time-dependent motion of passive elastic posts placed at different distances from the active post.

Data, Materials, and Software Availability. All study data are included in the article and/or supporting information.

ACKNOWLEDGMENTS. A.C.B. gratefully acknowledges the financial support from NSF under grant number 2234135 to develop the theoretical models and DOE under grant number DE-FG02-90ER45438 to develop the computational approach. We also acknowledge the computational facilities at the Center for Research Computing at the University of Pittsburgh.

Author affiliations: [a]Department of Chemical Engineering, University of Pittsburgh, Pittsburgh, PA 15261

1. X. He *et al.*, Synthetic homeostatic materials with chemo-mechano-chemical self-regulation. *Nature* **487**, 214–218 (2012).
2. B. Pokroy, S. H. Kang, L. Mahadevan, J. Aizenberg, Self-organization of a mesoscale bristle into ordered, hierarchical helical assemblies. *Science* **323**, 237–240 (2009).
3. Z. Wei *et al.*, Elastocapillary coalescence of plates and pillars. *Proc. R. Soc. A: Mathematical, Phys. Eng. Sci.* **471**, 20140593 (2015).
4. A. Laskar, O. E. Shklyaev, A. C. Balazs, Self-morphing, chemically driven gears and machines. *Matter* **4**, 600–617 (2021), 10.1016/j.matt.2020.11.014.
5. R. K. Manna, O. E. Shklyaev, A. C. Balazs, Chemically driven multimodal locomotion of active, flexible sheets. *Langmuir* **39**, 780–789 (2023), 10.1021/acs.langmuir.2c02666.
6. R. K. Manna, O. E. Shklyaev, A. C. Balazs, Chemical pumps and flexible sheets spontaneously form self-regulating oscillators in solution. *Proc. Natl. Acad. Sci. U.S.A.* **118**, e2022987118 (2021), 10.1073/pnas.2022987118.
7. R. K. Manna, O. E. Shklyaev, H. A. Stone, A. C. Balazs, Solutal-buoyancy-driven intertwining and rotation of patterned elastic sheets. *PNAS Nexus* **1**, 72 (2022), 10.1093/pnasnexus/pgac072.
8. R. K. Manna, O. E. Shklyaev, H. A. Stone, A. C. Balazs, Chemically controlled shape-morphing of elastic sheets. *Mater. Horizons* **7**, 2314–2327 (2020), 10.1039/d0mh00730g.
9. B. Evans *et al.*, Magnetically actuated nanorod arrays as biomimetic cilia. *Nano Lett.* **7**, 1428–1434 (2007).
10. M. Vilfan *et al.*, Self-assembled artificial cilia. *Proc. Natl Acad. Sci. U.S.A.* **107**, 1844–1847 (2010).
11. S. Khaderi *et al.*, Magnetically-actuated artificial cilia for microfluidic propulsion. *Lab on a Chip* **11**, 2002 (2011).
12. X. Dong *et al.*, Bioinspired cilia arrays with programmable nonreciprocal motion and metachronal coordination. *Sci. Adv.* **6**, eabc9323 (2020).
13. H. Sugioka, H. Yoshijima, Metachronal motion of artificial cilia using induced charge electro-osmosis. *Colloids Surfaces A: Physicochem. Eng. Aspects* **626**, 127023 (2021).
14. W. Wang *et al.*, Cilia metasurfaces for electronically programmable microfluidic manipulation. *Nature* **605**, 681–686 (2022).
15. J. den Toonder *et al.*, Artificial cilia for active micro-fluidic mixing. *Lab on a Chip* **8**, 533–541 (2008).
16. C. L. Van Oosten, C. W. Bastiaansen, D. J. Broer, Printed artificial cilia from liquid-crystal network actuators modularly driven by light. *Nat. Mater.* **8**, 677–682 (2009).
17. R. J. Raak, S. J. Houben, A. P. Schenning, D. J. Broer, Patterned and collective motion of densely packed tapered multiresponsive liquid crystal cilia. *Adv. Mater. Technol.* 7, 2270045 (2022).
18. S. Li *et al.*, Self-regulated non-reciprocal motions in single-material microstructures. *Nature* **605**, 76–83 (2022).
19. Z. Deng, H. Zhang, A. Priimagi, H. Zeng, Light-fueled nonreciprocal self-oscillators for fluidic transportation and coupling. *Adv. Mater.* 2209683 (2023).
20. L. Liu *et al.*, Light tracking and light guiding fiber arrays by adjusting the location of photoresponsive azobenzene in liquid crystal networks. *Adv. Optical Mater.* **8**, 2000732 (2020).
21. J. Bico, É. Reyssat, B. Roman, Elastocapillarity: When surface tension deforms elastic solids. *Annu. Rev. Fluid Mechanics* **50**, 629–659 (2018).
22. C. Ushay, E. Jambon-Puillet, P.-T. Brun, Interfacial flows past arrays of elastic fibers. *Phys. Rev. Fluids* **8**, 044001 (2023).
23. J. Cappello, B. Scheid, F. Brau, E. Siéfert, Bioinspired shape shifting of liquid-infused ribbed sheets. *Proc. Natl. Acad. Sci. U.S.A.* **120**, e2216001120 (2023).
24. R. Zhang, J. den Toonder, P. R. Onck, Transport and mixing by metachronal waves in nonreciprocal soft robotic pneumatic artificial cilia at low Reynolds numbers. *Phys. Fluids* **33**, 092009 (2021).
25. E. Milana, B. Gorissen, S. Peerlinck, M. De Volder, D. Reynaerts, Artificial soft cilia with asymmetric beating patterns for biomimetic low-Reynolds-number fluid propulsion. *Adv. Funct. Mater.* **29**, 1900462 (2019).
26. E. Milana *et al.*, Metachronal patterns in artificial cilia for low Reynolds number fluid propulsion. *Sci. Adv.* **6**, eabd2508 (2020).
27. H. Sugioka, M. Kubota, M. Tanaka, High-speed asymmetric motion of thermally actuated cilium. *J. Phys. Soc. Japan* **89**, 114402 (2020).
28. M. Lappa, W. Waris, On the role of heat source location and multiplicity in topographically controlled Marangoni–Rayleigh–Bénard convection. *J. Fluid Mechanics* **939**, A20 (2022).
29. S. Sengupta *et al.*, Self-powered enzyme micropumps. *Nat. Chem.* **6**, 415–422 (2014), 10.1038/nchem.
30. O. E. Shklyaev, H. Shum, A. Sen, A. C. Balazs, Harnessing surface-bound enzymatic reactions to organize microcapsules in solution. *Sci. Adv.* **2**, e1501835 (2016).
31. S. Lim, A. Ferent, X. S. Wang, C. S. Peskin, Dynamics of a closed rod with twist and bend in fluid. *SIAM J. Sci. Comput.* **31**, 273–302 (2008), 10.1137/070699780.
32. K. A. Johnson, R. S. Goody, The original Michaelis constant: Translation of the 1913 Michaelis-Menten paper. *Biochemistry* **50**, 8264–8269 (2011).
33. C. Chandrasekhar, *Hydrodynamic and Hydromagnetic Stability* (Clarendon Press, Oxford, 1961).
34. S. Das *et al.*, Harnessing catalytic pumps for directional delivery of microparticles in microchambers. *Nat. Commun.* **8**, 14384 (2017).
35. R. K. Manna, K. Gentile, O. E. Shklyaev, A. Sen, A. C. Balazs, Self-generated convective flows enhance the rates of chemical reactions. *Langmuir* **38**, 1432–1439 (2022), 10.1021/acs.langmuir.1c02593.
36. N. Lewis, S. Nathan, The caltech electronic nose project. *Eng. Sci.* **59**, 2–13 (1996).
37. C. Alexander, *A Pattern Language: Towns, Buildings, Construction* (Oxford University Press, 1977).
38. E. Schäffer, S. Harkema, M. Roerdink, R. Blossey, U. Steiner, Thermomechanical lithography: Pattern replication using a temperature gradient driven instability. *Adv. Mater.* **15**, 514–517 (2003).
39. E. McLeod, Y. Liu, S. M. Troian, Experimental verification of the formation mechanism for pillar arrays in nanofilms subject to large thermal gradients. *Phys. Rev. Lett.* **106**, 175501 (2011).
40. S. Succi, *The Lattice Boltzmann Equation: For Fluid Dynamics and Beyond* (Oxford University Press, 2001).
41. A. J. Ladd, R. Verberg, Lattice-Boltzmann simulations of particle-fluid suspensions. *J. Stat. Phys.* **104**, 1191–1251 (2001).
42. C. Pozrikidis, Shear flow over cylindrical rods attached to a substrate. *J. fluids Struct.* **26**, 393–405 (2010).

Downloaded from https://www.pnas.org by "UNIVERSITY OF PITTSBURGH, FALK LIBRARY /HEALTH SCIENCES" on March 12, 2025 from IP address 136.142.159.80.

43. C. Pozrikidis, Shear flow past slender elastic rods attached to a plane. *Intern. J. Solids Struct.* **48**, 137–143 (2011).
44. S. Gueron, N. Liron, Ciliary motion modeling, and dynamic multicilia interactions. *Biophys. J.* **63**, 1045–1058 (1992).
45. Y.-N. Young, M. Downs, C. R. Jacobs, Dynamics of the primary cilium in shear flow. *Biophys. J.* **103**, 629–639 (2012).
46. T. R. Powers, Dynamics of filaments and membranes in a viscous fluid. *Rev. Modern Phys.* **82**, 1607 (2010).
47. A.-K. Tornberg, M. J. Shelley, Simulating the dynamics and interactions of flexible fibers in Stokes flows. *J. Comput. Phys.* **196**, 8–40 (2004).
48. G. De Canio, E. Lauga, R. E. Goldstein, Spontaneous oscillations of elastic filaments induced by molecular motors. *J. R. Soc. Interface* **14**, 20170491 (2017).
49. F. Ling, H. Guo, E. Kanso, Instability-driven oscillations of elastic microfilaments. *J. R. Soc. Interface* **15**, 20180594 (2018).
50. C. H. Wiggins, D. Riveline, A. Ott, R. E. Goldstein, Trapping and wiggling: Elastohydrodynamics of driven microfilaments. *Biophys. J.* **74**, 1043–1060 (1998).
51. R. Cox, The motion of long slender bodies in a viscous fluid Part 1: General theory. *J. Fluid Mechanics* **44**, 791–810 (1970).
52. E. Lauga, T. R. Powers, The hydrodynamics of swimming microorganisms. *Rep. Prog. Phys.* **72**, 096601 (2009).
53. O. Du Roure, A. Lindner, E. N. Nazockdast, M. J. Shelley, Dynamics of flexible fibers in viscous flows and fluids. *Annu. Rev. Fluid Mechanics* **51**, 539–572 (2019).
54. N. Quennouz, M. Shelley, O. Du Roure, A. Lindner, Transport and buckling dynamics of an elastic fibre in a viscous cellular flow. *J. Fluid Mechanics* **769**, 387–402 (2015).
55. L. E. Becker, M. J. Shelley, Instability of elastic filaments in shear flow yields first-normal-stress differences. *Phys. Rev. Lett.* **87**, 198301 (2001).
56. N. Liron, S. Mochon, Stokes flow for a stokeslet between two parallel flat plates. *J. Eng. Mathematics* **10**, 287–303 (1976).

Downloaded from https://www.pnas.org by "UNIVERSITY OF PITTSBURGH, FALK LIBRARY /HEALTH SCIENCES" on March 12, 2025 from IP address 136.142.159.80.